

Harmonic Reflection Amplifier for Widespread Backscatter Internet-of-Things

Karan Gumber[✉], Member, IEEE, Corinne Dejous, Member, IEEE, and Simon Hemour[✉], Senior Member, IEEE

Abstract—The highly power-efficient backscattering communication scheme holds solid potentials to lead the Internet of Things technologies. However, the asymmetric radio frontend architectures that ensure cheap and pervasive communicating things and tags at one end of the link, overburden the other end of the link (“reader”) with complicated and expensive hardware. This turns out to prevent the integration of the technology in the wide spectrum of consumer electronic devices (e.g. RF smartphone platforms). By separating TX and RX frequency bands, the harmonic backscattering scheme drastically loosens the technological constraints toward integration. We propose here the use of a single tunnel diode to build a harmonic reflection amplifier (HRA), using the nonlinear behavior of the negative differential resistance region to both generate harmonics and amplify the signals. The circuit also behaves like a common backscatter, with the same-frequency backscattering modulation for operation with legacy readers. Operating below 150 mV, the HRA drains 144- μ W dc power with a measured positive conversion gain of 18 dB.

Index Terms—Backscatter radio, harmonic reflection amplifier (HRA), RFID, self-interference, tunnel diode.

I. INTRODUCTION

WITH the emergence of the fifth-generation (5G) technologies, the year 2020 came across 30 billion connected devices, or 5.1 connected devices per person on average [1], which anticipates a proliferation of Internet-of-Things (IoT) platforms that could range from small portable electronics devices such as smartphones and sensors to large electric vehicles. Backscatter communication is a promising technology toward true ubiquitous IoT, as it simplifies the many “thing” complexity [2]. In this asymmetric communication scheme, the RF signal is generated on one side only (the reader), whereas the tag backscatters the modulated signal to the reader with identification and other preferred information [3].

Most readers work in a monostatic configuration where a transmitter (Tx) and receiver (Rx) share the same antenna.

Manuscript received July 21, 2020; revised September 19, 2020 and October 27, 2020; accepted October 31, 2020. Date of publication December 1, 2020; date of current version January 5, 2021. This work was supported in part by the French State in the frame of the “Investments for the Future” Programme IdEx Bordeaux, under Grant ANR-10-IDEX-03-02 and in part by LabEx AMADEus under Grant ANR-10-LABX-0042-AMADEUS. (Corresponding authors: Simon Hemour; Karan Gumber.)

The authors are with the IMS Research Center, Department of Science and Technology, University of Bordeaux, Bordeaux INP, CNRS UMR 5218, 33400 Talence, France (e-mail: karan.gumber@u-bordeaux.fr; corinne.dejous@ims-bordeaux.fr; simon.hemour@u-bordeaux.fr).

Color versions of one or more figures in this article are available at <https://doi.org/10.1109/TMTT.2020.3038222>.

Digital Object Identifier 10.1109/TMTT.2020.3038222

The low Tx to Rx isolation resulting from contiguous intraband operation leads to self-interference (SI) or self-jamming signal leakage. Unfortunately, the antijamming interference circuits and/or high dynamic radio front end that have to be used to circumvent SI are expensive [4]. Self-jamming mitigation can either use interference from directional coupler [5] or quasi-circulator [6]. Substantial methods have been employed, including LNA postdistortion [7], feed-forward cancellation [8], and impedance tuning [9].

In [10], the mitigation of SI in the monostatic configuration is done by using a directional coupler with an impedance mismatch reflector incorporated into the antenna. Similarly, the antijamming signal in [11] has been achieved with the combination of a power divider, combiner, and vector multiplier. However, the performance of this method is entirely dependent on the dynamic range of the vector multiplier. To cancel the leakage signal in [12], a compensation signal was generated using an ultra-wideband poly-phase power divider, which is added vectorially before the receiver front end. Signal conditioning has been used in [13], in which a sample of Tx signal is combined with an Rx signal with opposite phase to counter the SI. The adaptive SI cancellation algorithm was discussed in [14] that automatically alters the self-jamming signal depending upon the changes in the tag environment.

All these methods provide rejection of the Tx leakage, but at the cost of increased reader Rx complexity. These solutions are also bulky in physical size and simultaneously limit the sensitivity of the system.

An alternative technique to reduce self-jamming is separating the Tx/Rx frequencies, similar to the frequency-division duplex system. The Tx leakage that influences the Rx frequency is filtered at Tx output, conversely, the leakage outside the Rx frequency is filtered at Rx input. Therefore, in recent years, alternative solutions have been exploiting passive transponders/tags [15], [16] to generate harmonics for enabling communication that greatly reduces direct reflections and self-interference. The idea has even been proposed for an active [17] circuit. However, dual-band operation is not new and has been explored for the RFID transponder [18]–[20], but the generation of harmonics comes at a cost of conversion loss that significantly impacts the link budget, and thus the communication distance. Table I and Fig. 1 compare the proposed outcome with the previously reported reflection amplifier in terms of power consumption, gain, and power-added efficiency (η) (PAE) [21]–[40], while Table II compares the performance of

TABLE I
COMPARISON OF STATE-OF-THE-ART REFLECTION AMPLIFIERS AVAILABLE IN LITERATURE

Ref.	Year	Device	Freq. (GHz)	V _{dc} (V)	I _{dc} (mA)	P _{dc} (mW)= V _{dc} *I _{dc}	P _{in} (dBm) or P-1 dB	Gain (dB)	P _{out} (dBm)= P _{in} +Gain	$\Delta\eta = \frac{P_{out}}{P_{dc}}$
This work	2020	AI301A GaAs Tunnel Diode	0.4146	0.144	1	0.144	-43	30	-13	34.79
			0.8292					20	-23	3.479
			CG**					16	-27	1.385
[21]	2019	NE3509M04 GaAs FET	2.45	1	--	--	--	11.5	--	--
[22]	2018	MBD5057-E28 Ge Tunnel Diode	5.8	0.09	0.5	0.045	-75	40	-35	0.702
[23]	2018	MBD5057-E28 Ge Tunnel Diode	5.8	0.06	0.34	0.0204	-81	35	-46	0.123
[24]	2017	NE3509M04 (Renesas) GaAs FET	1.8 2.4	1 2.4	2.4	2.4	-24.9 -24.8	21.9 13	-3 -11.8	20.87 2.7525
[25]	2017	AI301A GaAs Tunnel Diode	0.89	0.2	1	0.2	-30	17	-13	25.055
[26]	2017	AI201A GaAs Tunnel Diode	0.915	0.117	1.5	0.178	-30	13	-17	11.2
[27]	2017	2um Resonant Tunnel Diode	5.8	2*0.47	0.46	0.42	-34	8.6	-25.4	0.68
[28]	2015	MBD5057-E28 Ge Tunnel Diode	5.45	0.08	0.566	0.045	-70	34.4	-35.6	0.612
[29]	2014	BFT25A Bipolar Junction Transistor	0.915	0.755	0.431	0.325	-50 -40 -30	10.2 7.7 4.9	-39.8 -32.3 -25.1	0.0327 0.143 0.9508
[30]	2014	Bipolar Junction Transistor	0.9	0.83	0.73	0.605	-50 -30	30 14.92	-20	1.65 5.13
[31]	2014	BFT25A Bipolar Junction Transistor	0.9	0.83	0.8	0.664	-50 -20	29 9	-21	1.196 11.96
[32]	2014	InP 0.9um Resonant Tunnel Diode	5.7	0.36	0.173	0.125	--	10.4	--	--
[33]	2013	BPF405 (Infineon) Si BJT	5.25	2.5	0.8	2	-25	13	-12	3.15
[34]	2013	CFY30 MESFET	4.5	3	6	18	--	10.2	--	--
[35]	2013	Josephson junction	2.685	--	0.054	--	-117	30	-87	--
[36]	2012	MOSFET	4	0.8	0.15	0.12	-71.9	22.3	-49.6	0.00933
[37]	2011	NE32584 HJFET	5.8	0.7	9	6.3	--	11.48	--	--
[38]	2008	pHEMT	21	2.3	91	209.3	-75	14	-61	0
[39]	2006	pHEMT-MMIC DOIPH process	21	3	110	330	-45	14	-31	0.00024
[40]	2003	NE32584C HJFET	6.26	--	--	--	--	8.1	--	--

CG**= Conversion Gain @ $2f_0$:414.6MHz to 829.2MHz

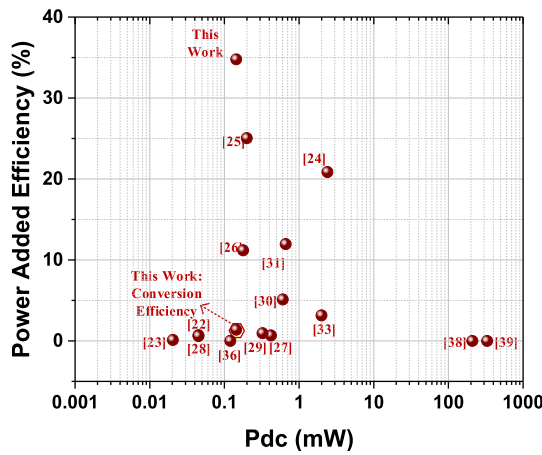


Fig. 1. Comparing the various state-of-the-art reflection amplifiers in terms of efficiency and output power versus dc power consumption.

the proposed harmonic backscatterer with previously reported harmonic tags [15], [19], [41]–[45].

A harmonic tunneling tag concept is illustrated in Fig. 2, where the tunnel diode is employed as a nonlinear element. The signal illuminates the tag at the fundamental frequency (f_0), and the nonlinear element in the tag generates

TABLE II
COMPARISON OF STATE-OF-THE-ART HARMONIC BACKSCATTER

Ref.	Type	2 nd Harmonic Freq. (GHz)	CG (dB)
This work	Active	0.414>0.829	-24 to +29
[15]	Passive	1.6	-26
[19]	Passive	7	-17
[41]	Passive Active	0.929	-15 (without amplifier) -8 (with amplifier)
[42]	Semi-passive	1.8	-23
[43]	Passive	2.4	-26.5
[44]	Passive	2	-19.9
[45]	Passive	1.736	-30

and re-radiates the signal back to the reader, both at the fundamental frequency (f_0) and the second harmonic ($2f_0$).

This article is an expanded version of [46], which proposed a topology based on a nonlinear, negative resistance-based tag that can completely overshadow the SI and also provide a conversion gain of around 18 dB at $2f_0$ with a power consumption of $144 \mu\text{W}$, measured at an excitation signal of -50 dBm . In addition, the HRA allows simultaneous use of both the frequency bands to enable legacy compatibility

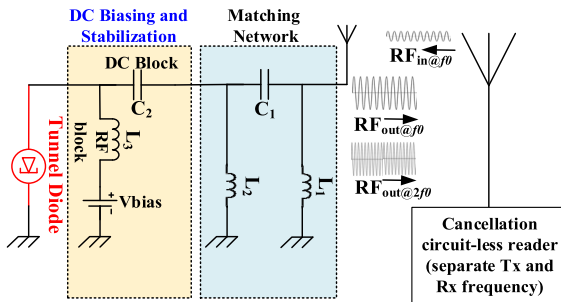


Fig. 2. Harmonic tunneling RFID dual-band communication system that is able to communicate at fundamental and harmonic frequency.

with nonharmonic readers. It also increases the throughput in a crowded frequency spectrum and thus it has emerged as a potential solution in a cluttered environment for long-range RFID tags.

The originality of the work lies in stability analysis of the proposed HRA. The concept of stability in negative resistance devices is explained theoretically and supported by simulation as well as measurement results. The capacity of the HRA to perform binary phase shift keying (BPSK) is also elaborated in the expanded version. In addition, the effect of the incident power on the reflection gain, conversion gain, and input impedance of the HRA are experimentally demonstrated. The impedance characterization of the AI301A bare tunnel diode in the simulations and measurements has been carried out.

This article is organized into five sections. Section II provides the details on the characterization of the bare tunnel diode, while Sections III and IV demonstrate the measurement results based on static and dynamic-bias modulation, respectively. Finally, based on analysis and preceding results, conclusions are made in Section V.

II. CHARACTERIZATION OF A BARE TUNNEL DIODE

The first step before fabricating any prototype based on a tunnel diode is to determine the dc current-voltage ($I-V$) characteristic of the bare tunnel diode. The dc $I-V$ characteristics of the three tunnel diodes (AI301A, 3I101D, and 3I306E) are shown in Fig. 3, and they are measured over a bias voltage (V_b) ranging from 0 to 300 mV. The differential resistance and current responsivity [47] of AI301A are also shown in Fig. 3. Table III shows a comparison of these three diodes based on SPICE parameters, each with its biasing voltage and the corresponding negative.

As depicted from the $I-V$ curve, the tunnel diode AI301A shows a negative differential resistance (NDR) region from 110 to 300 mV, where the output current starts reducing with the increase in V_b . When biased in the NDR region, the tunnel diode can operate as an amplifier. For a given dc bias (meaning dc power loss), a positive differential resistance would dissipate RF power ($R\dot{I}^2$), while a negative differential resistance would increase RF power ($-R\dot{I}^2$) and this property makes it different from other diodes.

For these measurements, the E3648A high precision biasing supply from Keysight is used to bias the diode, which was controlled using the Command Expert, Standard Commands

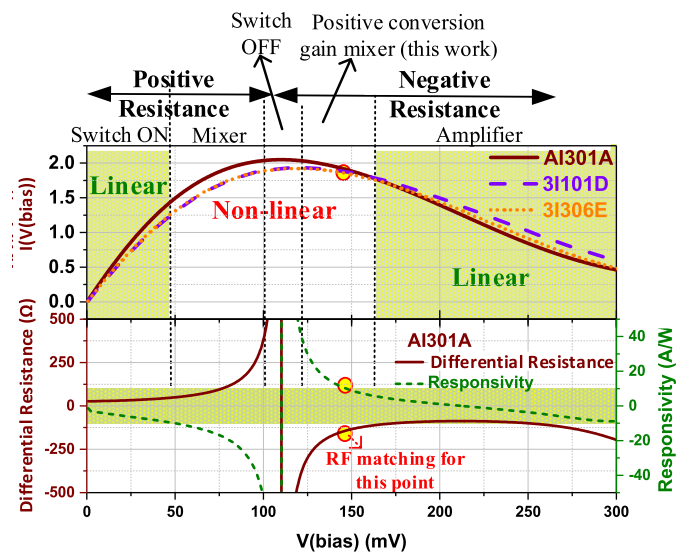


Fig. 3. Measured dc characteristics of the tunnel diodes AI301A, 3I101D and 3I306E. The seventh-order polynomial fitting of the measured dc $I-V$ characteristic allowed to estimate the differential resistance of AI301A $| - R_{td} | = 147 \Omega$ and the responsivity $\mathfrak{R} = 11.9 \text{ A/W}$ that are highlighted, for biasing at 144 mV. Shaded region represents linear characteristics, where $\mathfrak{R} \leq 7.5 \text{ A/W}$.

TABLE III
PERFORMANCE COMPARISON OF THREE DIFFERENT TUNNEL DIODES

Parameters	Circuit I-AI301A	Circuit II-3I101D	Circuit III-3I306E
Vbias (mV)	144	214	164.5
I(Vbias) (mA)	1	0.68	1.073
Power consumed (uW)	144	145.5	176.5
Negative resistance	-147	-158	-137
Peak current @25°C	1.6 – 2.4 mA	1.7 – 2.4mA	1.8 – 2.2mA
Voltage at peak current	<180mV	<160mV	<170mV
Parasitic capacitance	< 12 pF	2.5 – 10pF	4 – 12pF
Parasitic inductance	<1.5nH	<1.3nH	NA
technology	GaAs	GaAs	GaAs

for Programmable Instruments. For high precision extraction of voltage and current consumption of AI301A tunnel diode, 34410 and 34401 digital multimeters (DMM) are employed. The number of power line cycles (PLCs) of 34410 DMM is set to 10, and 34401 DMM is set to six digits slow, which corresponds to 100 PLC integration time and 6.5-digit resolution. The biasing voltage across the diode is varied from 1 mV to 300 mV at a step of 1 mV, and the delay between two consecutive steps is set to 3 s

$$I(v) = \sum_{i=0}^{i=N} a_i v^i, \quad N \in \mathbb{N}. \quad (1)$$

The seventh-order polynomial fitting was extrapolated [48]

$$I(v) = -5.83v^7 + 14.12v^6 - 12.87v^5 + 5.10v^4 - 0.53v^3 - 0.18v^2 + 0.04v - 1.47 \cdot 10^{-5}. \quad (2)$$

Over the negative R_{td} region (Fig. 3) the device exhibits a peak-valley voltage (ΔV) and current (ΔI) difference of around 190 mV and 1.62 mA, respectively, which sets the

maximum RF “output” power of the diode to about -12 dBm, as calculated from [49]

$$P_{\max} = \frac{3}{16} \Delta V \Delta I. \quad (3)$$

Frequency multiplication can be obtained when the NDR varies nonlinearly with the voltage. The optimum doubler efficiency can be obtained, when the diode is biased at the edge of the NDR region, as the $I-V$ characteristic is almost symmetrical at the bias point [50] and the current responsivity is high. Alternately, biasing the device at the NDR midrange, anti-symmetrical around the bias point, with a constant value of R_{td} and lower responsivity absolute value, would lead to the highest tripling efficiency. In this work, aiming at a doubler amplifier, the bias point was chosen as 144 mV, $| -R_{\text{td}} | = 147 \Omega$. Operating on the peak current, $V_b = 110$ mV, $| -R_{\text{td}} | > 1500 \Omega$, offers no advantage as suggested in [51].

III. HARMONIC TUNNELING TAG STATIC MEASUREMENT

The measurement campaign aimed to experimentally validate the capacity of the harmonic tunneling tag in terms of achievable reflection gain at the fundamental frequency and conversion gain at the second harmonic. The basis of any measurement relies on its simulation framework, which is elaborated first.

A. Simulation Framework

The simulation work of the proposed design is carried out in the advance design system (ADS) by building the symbolically defined device (SDD) model of tunnel diode from its $I-V$ characteristics. The transient simulations are performed to make sure that the HRA does not start to oscillate at any biasing voltage. The matching network was built to obtain the desired output signal at the frequency of interest. The matching network includes a dual-band LC resonator indicated in Fig. 2. The matching network performs two functions (a) make sure that the negative impedance of the diode is successfully transformed into antenna impedance and (b) ensure the selectivity of the desired dual-frequency band. The negative resistance seen toward the diode is -147Ω , and the input impedance of the HRA is approx. -49Ω , when the incident power is -60 dBm. This impedance transformation is carried by the matching circuit to ensure stability as well as to transfer maximum power.

The simulated S-parameters of the full circuit (excluding diode) are shown in Fig. 5. The circuit has been optimized to exhibit negative resistance at only 450- and 900-MHz frequencies. Simulation is then compared to S1P (one-port S parameter) measurements of the physical tunnel diode at the optimum bias point.

The performance of the overall HRA is characterized by reflection gain, which is given as

$$|\Gamma_{\text{in}}|^2 = \left| \frac{Z_{\text{diode}} - Z_{\text{circuit}}}{Z_{\text{diode}} + Z_{\text{circuit}}} \right|^2 \quad (4)$$

where Z_{circuit} is the load impedance connected to the reflection amplifier. Note that the Z_{circuit} should also consider the antenna

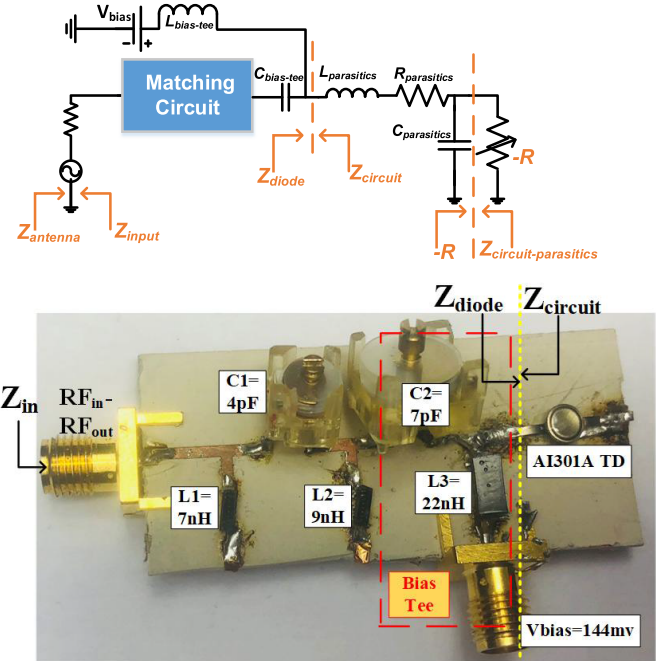


Fig. 4. Fundamental block diagram and fabricated prototype of a harmonic reflection amplifier.

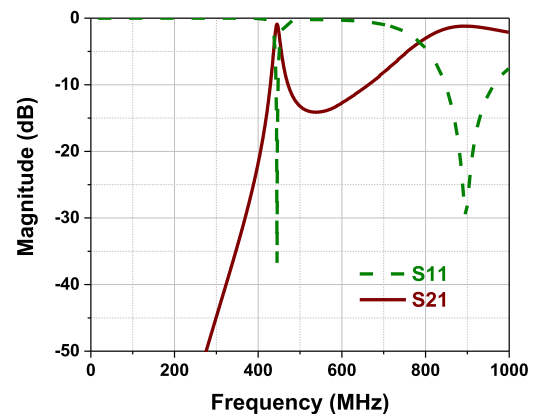


Fig. 5. Simulated S-parameter of circuit without tunnel diode, representing two resonances at the desired frequency band.

impedance at the input port; Z_{diode} is the input impedance of the tunnel diode (Fig. 4). The reflection gain of HRA must exceed unity as the input resistance of the tunnel diode is negative [52]. If Z_{diode} approaches $-Z_{\text{circuit}}$, then Γ_{in}^2 tends to infinity. Oscillations can start if the magnitude of the negative impedance of the diode exceeds the magnitude of the positive load impedance of the circuit [53], [54]

$$\text{Re}[Z_{\text{circuit}}] \leq |\text{Re}[Z_{\text{diode}}]| \quad (5)$$

where $\text{Re}[Z_{\text{diode}}] < 0$. To avoid such uncontrolled oscillations, the load impedance magnitude of the circuit designed must be always greater than the negative impedance magnitude of the diode, which is given by

$$\text{Re}[Z_{\text{circuit}}] - |\text{Re}[Z_{\text{diode}}]| > 0 \quad (6)$$

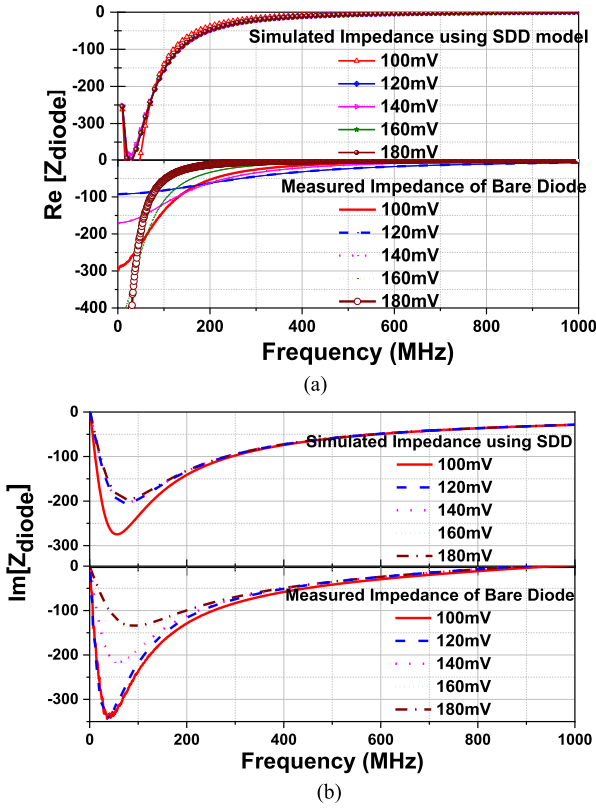


Fig. 6. (a) Real and (b) imaginary impedances of the tunnel diode at various biasing using the simulated SDD model, and measured AI301A bare diode.

where $\text{Re}[Z_{\text{diode}}] < 0$, and the highest reflective gain is obtained only if $|\text{Re}[Z_{\text{diode}}]|$ is kept different from $\text{Re}[Z_{\text{circuit}}]$ by a very small margin.

The simulated real and imaginary impedances of the tunnel diode SDD model at different bias points are shown in the top graph of Fig. 6(a) and (b), respectively. Quite a good agreement is observed with the measured real and imaginary impedances of the AI301A tunnel diode represented in the bottom graph of Fig. 6(a) and (b).

In order to achieve high gain at the frequency of interest, the impedance of the matching network is tuned very close to the negative input impedance of the tunnel diode, while respecting the nonoscillation conditions.

B. Experimental Setup

For prototyping and testing, the AI301A soviet tunnel diode is used which is cheap, rugged, and easily available. It is also important to mention that more efficient tunnel diodes can operate at a lower biasing point. The experimental prototype of the proposed circuit can be seen in Fig. 4(b). It was fabricated using Rogers RO3010 substrate with a thickness of 1.28 mm, a dissipation factor of 0.0022, and a relative permittivity of 10.2. The fabricated hardware was composed of an AI301A tunnel diode, variable capacitances from Vishay, and inductors from Coilcraft.

The various components of the HRA are tuned and optimized using harmonic balance and transient simulation in ADS to ensure maximum reflection and conversion gain at

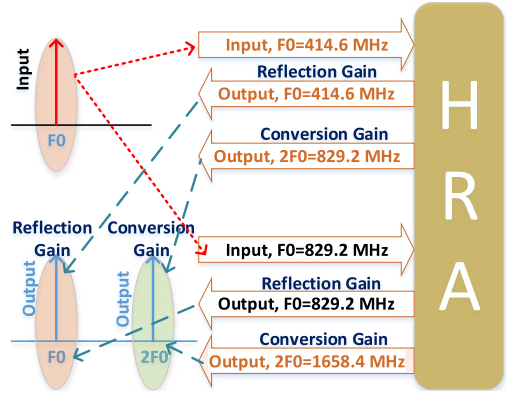


Fig. 7. Basic working principle of the harmonic reflection amplifier.

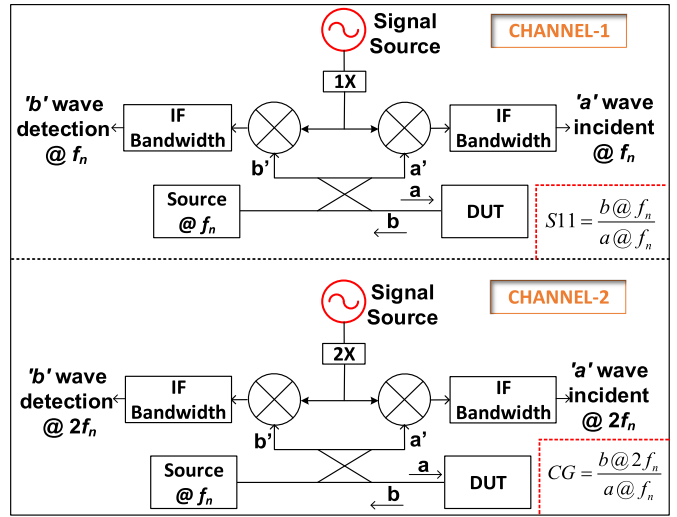


Fig. 8. Block diagram of one port network analysis, showing two channels with “*a*,” “*b*” waves that measure the incident ($@f_n$) and reflected ($@f_n$ and $@2f_n$) waves.

a fundamental and second harmonic frequency, while at the same time disabling the oscillatory conditions. The working operation of HRA is summarized in Fig. 7.

The type of operation performed by the HRA depends on the input signal. With a single frequency band at f_0 , which can either be centered at 414.6 or 829.2 MHz, the amplifier performs a dual-band operation, by boosting the signal at fundamental frequency f_0 , and the second harmonic frequency.

For such characterization, a one-port network analysis with frequency offset is performed (Fig. 8). Since one-port conversion gain is usually not available on a vector network analyzer, it has to be computed from the raw $f_n a$ wave (measurements at f_n with a source at f_n), and the $2f_n b$ wave (measurements at $2f_n$ with source at f_n). Note that special care should be given in the calibration and error coefficient handling, as the forward error term should be taken into account at f_n , while the reverse wave error term should be considered at $2f_n$. Conversion gain for higher harmonics follows the same methodology. Practically, these measurements are done with Keysight E5080 vector network analyzer (VNA), for incident power ranging from $P_{\text{in},\text{min}} = -90 \text{ dBm}$ to $P_{\text{in},\text{max}} = -20 \text{ dBm}$.

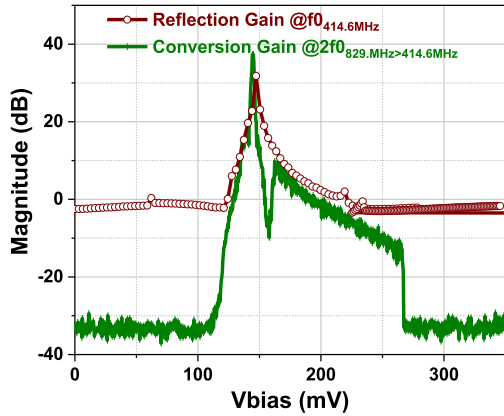


Fig. 9. Measured reflection and conversion gain as a function of the bias voltage for an input frequency of 414.6 MHz and an input power of -50 dBm.

C. Tuning the Negative Differential Resistance and the Conversion Gain

The negative resistance of the tunnel diode is exploited with respect to biasing voltage. The change in the biasing voltage tunes the negative differential resistance of the tunnel diode, which in turn produces the reflection and conversion gain. The gains as a function of biasing voltage are shown in Fig. 9.

As depicted in Fig. 9, one can easily achieve the desired gain just by tuning the biasing voltage. This experiment is conducted to show the reproducibility of the measurement results across different tunnel diodes (same part number). If any other diode with the same part number is employed it can produce similar results but maybe with a change in the bias point.

D. Frequency Behavior and Stability Conditions

The optimum behavior of the proposed HRA is found for a bias voltage of $V_b = 144$ mV. Under this dc condition, the measured input impedance of the bare AI301A tunnel diode is

$$Z_{\text{diode}} = \begin{cases} -27 - j \times 44 \Omega @ f_0 = 414.6 \text{ MHz} \\ -8 - j \times 4 \Omega @ 2f_0 = 829.2 \text{ MHz} \end{cases}.$$

To assess the overall stability of the circuit, the input impedance has to be measured as seen from the antenna to verify that there is no frequency for which it goes to the instability region. The stability test is conducted in Fig. 10, where the real impedance of the HRA is plotted against incident power. As shown in Fig. 10, when the incident power approaches near -50 dBm, the HRA impedance reduces from -50Ω toward the instability region.

It can also be confirmed from Fig. 11 that shows the measured real part of the HRA impedance for an incident power of -50 dBm before final tuning. It is observed that two sharp resonances with values below -50Ω at f_0 , approximately -48Ω at $2f_0$. Under such conditions, free-running oscillation would occur at f_0 , while an incident signal at the vicinity of f_0 would trigger an injection-locked oscillation [55]–[57].

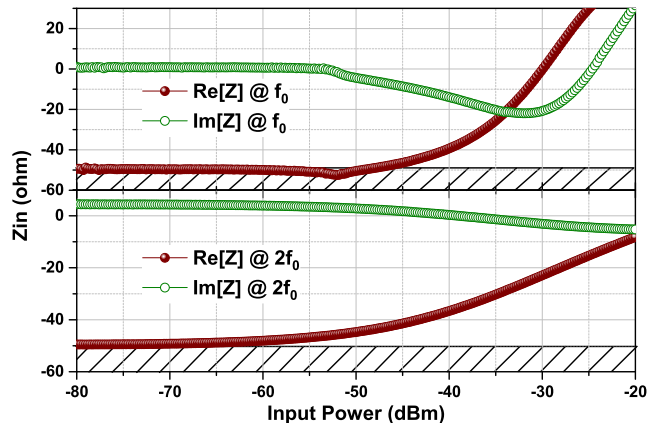


Fig. 10. Measured real (brown) and imaginary parts (green) of the HRA impedance at both frequencies f_0 ($=414.6$ MHz) and $2f_0$ ($=829.2$ MHz) for various incident powers, when optimum bias of 144 mV is applied.

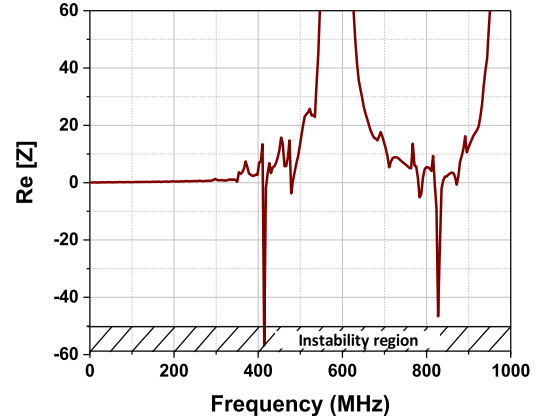


Fig. 11. Measured input impedance of the HRA before final biasing for an incident power of -50 dBm, when an optimum bias of 144 mV is applied. Under such conditions, self-injection locking would be expected at f_0 , because the impedance of the HRA falls below -50Ω . The shaded portion represents the unstable region, if the antenna impedance (Z_{antenna}) = 50Ω .

E. Antenna Impedance Impact on the Operation

The antenna impedance mostly varies in practical case toward higher real impedance value because equivalent series resistance increases with the added loss of the surrounding antenna. Therefore, there is no risk for instability if the surrounding happened to impact the antenna impedance. Fig. 12 shows the impact of antenna impedance on the stability of the proposed HRA. It can be observed from the contour plot, that the HRA always remains stable if the antenna impedance is higher than 50Ω . If the antenna impedance is close to 50Ω , it yields the maximum reflection gain (as high as 30 dB).

F. Influence of the Incident Power on Stability

As the HRA is designed to operate at a negative impedance very close to the antenna impedance, it is also necessary to verify the stability versus incident signal RF power level. It can be explained by considering Figs. 10 and 13, where Fig. 10 represents the variation of real and imaginary parts of the HRA input impedance at both frequencies as a function of the incident power level.

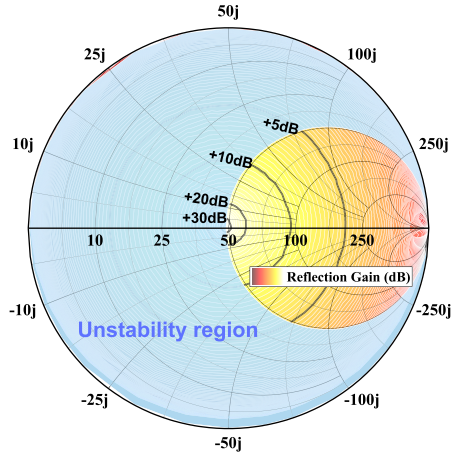


Fig. 12. Contour chart of the reflection gain (4) and stability criteria (5) for a source-pull calculation of any possible antenna impedance considering the input impedance ($47-j \times 1.3 \Omega$) of the circuit at 414 MHz for power below -60 dBm.

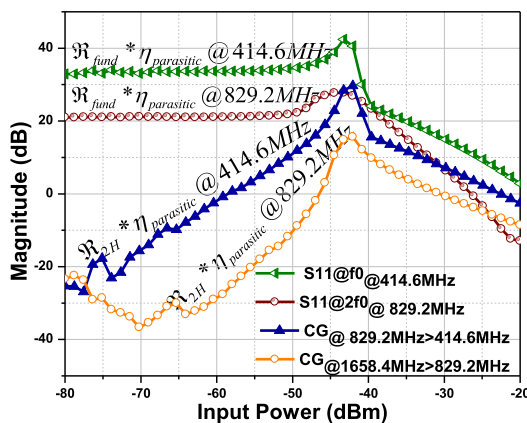


Fig. 13. Measured input reflection coefficient (S11) at fundamental frequency f_0 (green), and at $2f_0$ (brown), and second harmonic conversion gains with respect to f_0 (blue) and $2f_0$ (orange) as a function of incident RF power.

This can be observed in Fig. 13, which depicts the reflection gain (S11) and conversion gain of the HRA as a function of the incident power. From very low incident power (-90 dBm) to -50 dBm, the equivalent (linear) resistance seen by the input signal is very close to -50Ω , related to a high and constant value of S11. Note that in the case of unstable behavior, the S11 would keep rising as the incident power increases.

Furthermore, it can be observed in Fig. 13 that near -50 dBm, the reflection gains at f_0 and $2f_0$ are maximum, as well as the conversion gains at both frequencies. It happens because $\text{Re}[Z_{\text{diode}}]$ comes very close to $\text{Re}[Z_{\text{circuit}}]$, that provides high reflective gain \tilde{A}_{in} as indicated in (4). Beyond -50 -dBm incident power level, the real part of the impedance at f_0 and $2f_0$ increases from -50Ω and mismatch takes place, (shown in Figs. 10 and 11). The higher the mismatch of real impedance, the lower the reflection and conversion gains.

Both reflection and conversion gains originate from different physical mechanisms of the tunnel diode. The conversion gain results from the fast varying input impedance, which is linked to the second-order $I(V)$ curve variation, i.e., the dc current

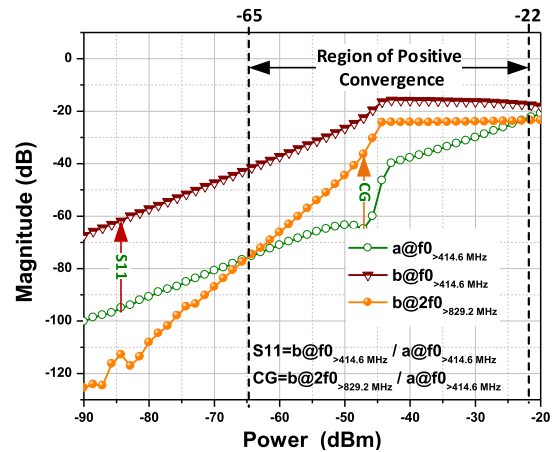


Fig. 14. One port analysis of the HRA to find reflection and conversion gains from “a,” “b” waves at fundamental frequency $f_0 = 414.6$ MHz.

responsivity represented in Fig. 3. Thus, the nonlinearity of tunnel diode generates the inter-modulation product and higher harmonics, which is power-dependent, since more incident RF power will lead to greater impedance variation, hence more conversion. The negative input impedance of the circuit (linked to the differential resistance of the tunnel diode) is responsible for amplification of every existing signal, i.e., for the incident wave (reflection gain) as well as the generated harmonics (conversion gain).

Of course, as the frequency increases, the signal is more subject to parasitic losses which lead to lower conversion gain, as is the case for 829.2 to 1658.4 MHz conversion gain. The measurements reported in Fig. 13 are used to investigate the P1-dB and P3-dB compression points. The measured P1-dB incident power $P_{\text{in-1 dB}}$ of -43 dBm at f_0 and $2f_0$ corresponds to a maximum linear Pout of -13 and -23 dBm, respectively.

The one port analysis of the HRA consistent with “a,” “b” waves at the frequency band $f_0 = 414.6$ MHz and exploiting the frequency offset mode with a multiplicative factor of 2 is shown in Fig. 14. The “a” and “b” wave centered at $f_0 = 414.6$ MHz are measured in Channel I corresponding to Fig. 8, whereas “b” wave centered at $2f_0 = 829.2$ MHz is measured in Channel II by exploiting frequency offset mode. The data extracted from these three waves help to find the reflection and conversion gains as depicted in Fig. 15. Both “a” and “b” show a very linear behavior from very low incident power (-90 dBm) to -50 dBm, that imply constant reflection gain (S11) in this region.

The conversion efficiency is given as a ratio of $b@2f_0 / a@f_0$. As is shown in Fig. 14 when “b” wave at $2f_0$ starts increasing from “a” wave at f_0 , it is marked as the region of positive conversion gain for second harmonic that lies at 829.2 MHz. This region starts originating when the incident power impinging on the HRA comes close to -65 dBm, and it continues up to -22 dBm incident power. Similarly, this positive region of conversion gain for the 829.2-MHz fundamental frequency that corresponds to the second harmonic at 1658.4 MHz is shown in Fig. 13. This region is very small, it is only restricted to the incident power ranging from

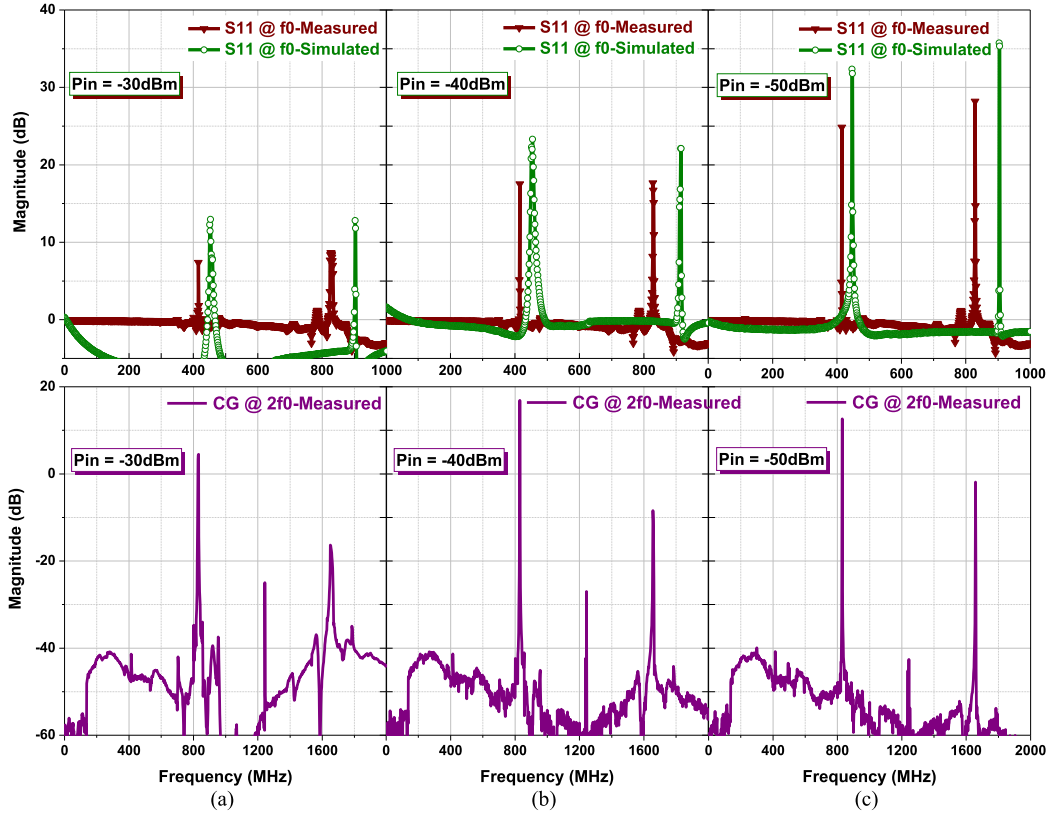


Fig. 15. Simulated (green) and measured (brown) reflection gain at fundamental frequency and measured conversion gain (purple) at the second harmonic frequency for the incident power (P_{in}) of (a) -30 dBm, (b) -40 dBm, and (c) -50 dBm. In the conversion gain graph, the frequency in x -axis is the frequency of the output signal.

-47 to -43 dBm, where the conversion gain at the second harmonic that lies at 1658.4 MHz goes above 0 dB.

Indeed, when the incident power is large enough, (here from -50 dBm), the tunnel diode ceases to operate in “small signal,” the input signal starts flowing over the positive resistance part of the curve and does not benefit further from the ideal (nonlinear and negative) response. This in turn modifies both the gain and input impedance of the HRA that pushes HRA into saturation and leads to a decrease of the gains.

It was observed that the HRA exhibits a reflection gain over the dual-frequency band. The measured reflection and conversion gains for three incident powers are shown in Fig. 15. It is observed that a peak reflection gain of 25 dB or even greater over both the frequency bands (f_0 and $2f_0$) at incident power of -50 dBm. At the same incident power, it provides a controllable conversion gain at the second harmonic of approximately 18 dB and -16.5 dB at 829.2 and 1658.4 MHz, respectively.

G. Selection of Device

The selection of the device is of concern for the fabrication of the amplifier, where stability is of paramount importance. Three different diodes are shortlisted for the purpose of fabricating an amplifier, which has very similar $I-V$ characteristics as depicted in Fig. 3. After fabricating the three prototypes with three different diodes, we found the 3I101D provides

excellent reflection as well as conversion gain. While, conducting the stability test, it is unstable starting from very low power to -40 dBm, which can be observed from Fig. 16. The other diode 3I306E passed the stability test as shown in Fig. 16, but was unable to provide good reflection and conversion gain. Therefore, the AI301A was chosen that has a combination of both stability and efficiency. To verify the reproducibility of measurement results across different AI301A tunnel diodes (using the same part number), two additional prototypes were tested using AI301A. All the prototypes tested using AI301A were very stable and produced good reflection and conversion gain.

H. Power Link Budget

The link budget is a method to diagnose the entire system. It determines the gain and losses in a system by calculating the RF power level at each point [58]. It governs the margin in system performance and can locate the point of failure. The evaluation of the proposed system is performed in two cases shown in Fig. 17. In Case I [shown in Fig. 17(a)], the reader and tag both transmit and receive fundamental frequency i.e. 414.6 MHz. However, in case II [shown in Fig. 17(b)], the reader illuminates the tag at the fundamental frequency, while the tag re-radiates the second harmonic, i.e. 829.2 MHz, to the reader. The power link budget of the entire system in

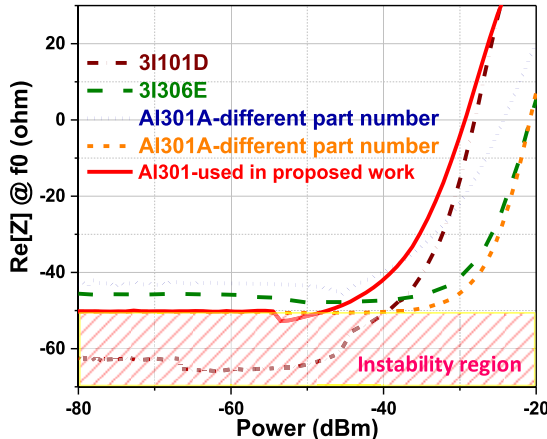


Fig. 16. Measured real impedance of the HRA for three different prototypes (employing different tunnel diodes at frequency f_0 ($=414.6$ MHz) for various incident powers.

TABLE IV

DESCRIPTION OF VARIOUS LINK BUDGET COMPONENTS

Link	Budget component	Term.	Value
Forw ard	Power transmit by reader	P_T	15dBm
	Reader antenna gain	G_R	4dBi
	Free space loss @ 414.6 MHz =	L_{FS} @414.6MHz	
	-27.55+20log(MHz)+20log(metre)		
Power incident at tag (P_{inc}) = $P_T + G_R - L_{FS}$ @414.6MHz			
Reve rse (Tag to reader)	Tag antenna gain	G_T	2dBi
	Miscellaneous Loss at tag	L_T	1dB
	Modulation Loss	P_{mod}	6dB
	<i>Case I:</i> Reflection gain provided by the HRA @ 414.6 MHz	G_{HRA} @414.6MHz	Fig. 13 (green)
<i>Case II:</i> Conversion gain provided by the HRA @ 829.2 MHz			
<i>Case I:</i> Free Path loss @ 414.6 MHz			
<i>Case I:</i> Free Path loss @ 829.2 MHz			
<i>Case I:</i> Power back to reader (P_{read}) @ 414.6 MHz			
$P_{read} = P_{inc} + G_T - L_T - P_{mod} - L_{FS}$ @414.6MHz + G_{HRA} @414.6MHz(RG)			
<i>Case II:</i> Power back to reader (P_{read}) @ 829.2 MHz			
$P_{read} = P_{inc} + G_T - L_T - P_{mod} - L_{FS}$ @829.2MHz + G_{HRA} @829.2MHz>414.6MHz(CG)			

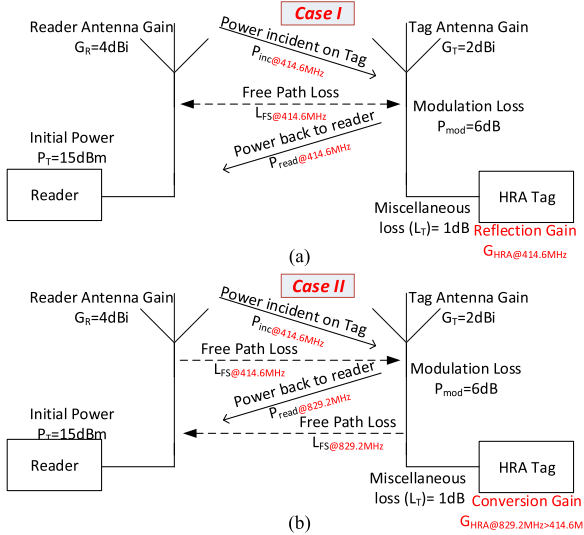


Fig. 17. Complete system for calculating the power link budget in the forward and reverse path. (a) Case I: reader transmits f_0 (414.6 MHz) and tag re-radiates f_0 (414.6 MHz), where tag provides reflection gain. (b) Case II: reader transmits f_0 (414.6 MHz) and tag re-radiates $2f_0$ (829.2 MHz), where tag provides conversion gain.

both cases is shown in Fig. 18, which is given as

$$P_{read} = P_T + G_R + G_T - L_T - P_{mod} - L_{FS} + G_{HRA} \quad (7)$$

all the above terms are explained in Table IV, where the value of the first five terms are assumed, the sixth term L_{FS} is calculated using the free-space path loss (FSL) equation provided in Table IV, and the value of the last term is extracted from Fig. 13. The fifth term, modulation loss (P_{mod}) occurs due to the change in circuit impedance from state “0” ($Z = 5.6-j \times 0.2 \Omega$) to state “1” ($Z = -51.6-j \times 3.2 \Omega$), which defines how the tag modulates the reader signal back to reader. The last term, gain provided by the HRA also depends upon the type of operation. If the system is operating as Case I [Fig. 17(a)], HRA provides reflection gain, whereas, if the

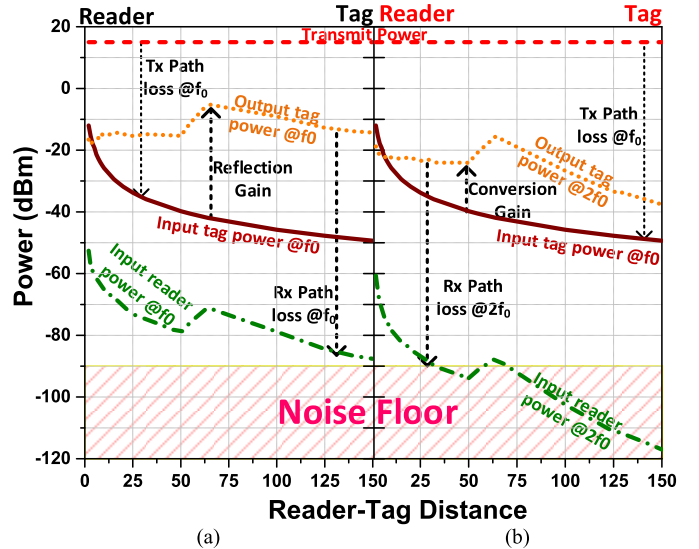


Fig. 18. Forward and backward link budget for active RFID communication system (a) corresponds to Fig. 17(a) and (b) corresponds to Fig. 17(b).

system is operating as Case II [Fig. 17(b)], HRA provides conversion gain.

Equation (7) is used to calculate the maximum read range of the complete system, which also depends on the readers receive sensitivity. The reader sensitivity is good enough so that the signal reflected by the tag must be successfully detected by the reader. For the proposed link budget, we assume readers receive sensitivity is around -90 dBm. The maximum theoretical read range of active HRA is around 150 and 35 m, which is shown in Fig. 18(a) and (b), corresponding to case I [Fig. 17(a)] and case II [Fig. 17(b)], respectively.

IV. HARMONIC TUNNELING TAG DYNAMIC MODULATION

The inherent negative resistance of tunnel diode enables HRA to be employed as a high gain modulator in backscattered

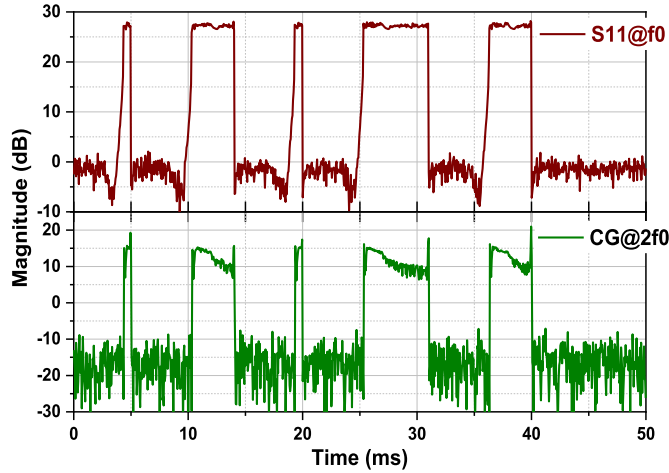


Fig. 19. Relative output power (reflection gain) corresponding to an arbitrary bit sequence OOK modulation at $f_0 = 414.6$ MHz, the “0” state corresponds to circuit impedance $Z = 5.6-j \times 0.2$ Ω , whereas the “1” state corresponds to $Z = -51.6-j \times 3.2$ Ω (top graph) and relative output power at $2f_0 = 829.2$ MHz (conversion gain) where the “1” corresponds to the input power at the fundamental being converted to the second harmonic frequency (bottom graph). The “0” state corresponds to no bias voltage, whereas the “1” state corresponds to 144 mV.

low powered RFID systems. We introduced a dual-band reflection amplifier in the previous section, it can modulate the backscatter signal by ON-OFF keying (OOK). It is more spectrally efficient than frequency shift keying, as no energy is spent on the transmission of zero, but it is more prone to noise and interferences [59], [60].

In the proposed HRA, both the frequency bands are either ON or OFF simultaneously, leading to compatibility with a legacy system that does not operate using harmonic backscatter communication. The response of the HRA to the arbitrary waveform 0101101011101100 OOK modulation is shown in Fig. 19 with an incident wave power of -50 dBm. It can be seen that the reflected power at fundamental frequency alternates between 0 and 28 dBm, which leads to a more than 25 dB contrast between the ON-OFF states. Moreover, the wave generated from the fundamental at the second harmonic alternates at -20 and 10 dBm, which means that even higher contrast is obtained. More contrast means the signal offers higher immunity to noise and interfering signals.

Phase shift keying (PSK) modulation can also be considered allowing constant power to be transferred to the transponder regardless of modulation state [61]. More specifically, BPSK is guaranteed with this circuit, as two phases of responses are obtained for the same gain. The phase of the backscatter signal and reflection gain at f_0 for the incident power of -50 dBm is shown in Fig. 20.

For Fig. 20, since the VNA could not control the dc bias, an indirect measurement was performed. The bias generator was set to bias the HRA with slow ramp function from 0 to 300 mV, while VNA measurements have been done in the time domain (thus on exact time corresponds to an exact bias). It is shown that a gain of 16.8 dB can be obtained for two different bias ($\phi = -97^\circ$ when $V_b = 142$ mV and $\phi = 83^\circ$, when $V_b = 146$ mV).

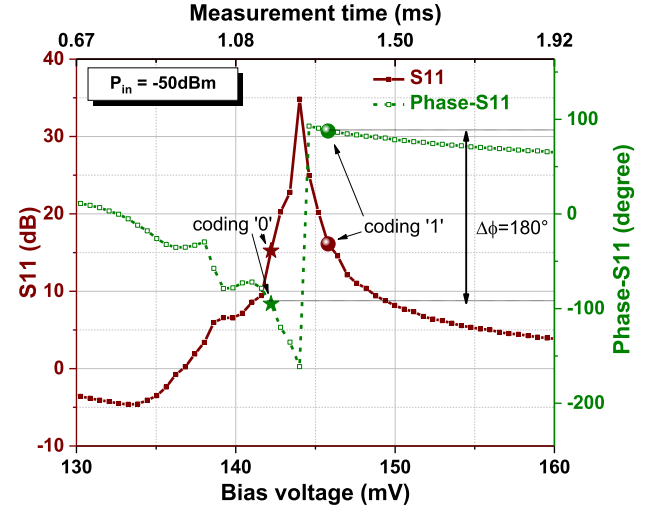


Fig. 20. Capability of the HRA to perform BPSK by maintaining the magnitude symmetry of 16.8 dB, but with a phase difference of 180° , at two different biasing points $V_{b1} = 142$ mV ($T_1 = 1.262$ ms) and $V_{b2} = 146$ mV ($T_2 = 1.277$ ms), respectively.

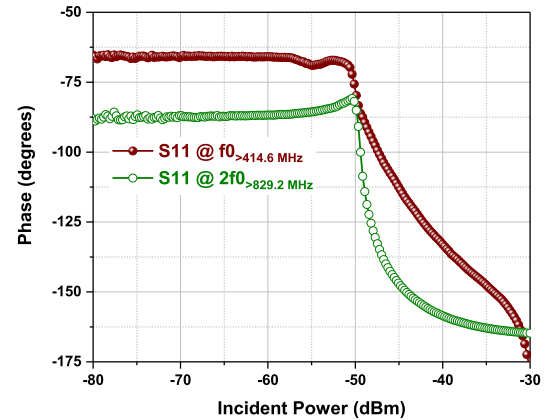


Fig. 21. Measured phase of the HRA at both frequency bands, $f_0 = 414.6$ MHz (wine) and at $2f_0 = 829.2$ MHz (green) for various incident power, when optimum bias of 144 mV is applied.

The phase stability as a function of the incident power is also measured to evaluate the impact of backscattering resilience to channel variation (Fig. 21). It is seen that the phase is quite stable at both frequencies.

V. CONCLUSION

This work describes the design and testing of a harmonic reflection amplifier using a tunnel diode that can amplify, backscatter, and modulate the incident RF power in legacy RFID applications. It also operates in dual-band for transmitting information using the inherently generated second harmonic. Its ability to operate in dual-band improves the sensitivity of a communication link by avoiding the self-jamming leakage and also acts smartly in a crowded frequency spectrum. The demonstrated HRA is ideally suited for RFID applications that deserve high data rates with improved read range. The conversion gain as high as +18 dB at the second harmonic opens up the way to integrate the proposed tunneling

tag with interband mobile communication. The low power consumption and considerable reflection/conversion gains make the proposed HRA an idyllic candidate for RFID and interband 5G communication.

REFERENCES

- [1] Cloud the Report. (Jul. 2018). *Red Pixie—The World of Data Infographic Black and Blue*. [Online]. Available: <https://www.redpixie.com/hubfs/Red%20Pixie%20-%20The%20World%20of%20Data%20infographic%20Black%20and%20Blue.pdf>
- [2] X. Gu, S. Hemour, and K. Wu, "Reconfigurable nonlinear circuit for wireless power harvesting and backscattering," in *Proc. 49th Eur. Microw. Conf. (EuMC)*, Paris, France, Oct. 2019, pp. 543–546.
- [3] A. Ramos, A. Lazaro, and D. Girbau, "Semi-passive time-domain UWB RFID system," *IEEE Trans. Microw. Theory Techn.*, vol. 61, no. 4, pp. 1700–1708, Apr. 2013.
- [4] A. Boaventura, J. Santos, A. Oliveira, and N. B. Carvalho, "Perfect isolation: Dealing with self-jamming in passive RFID systems," *IEEE Microw. Mag.*, vol. 17, no. 11, pp. 20–39, Nov. 2016.
- [5] W.-K. Kim *et al.*, "A passive circulator with high isolation using a directional coupler for RFID," in *IEEE MTT-S Int. Microw. Symp. Dig.*, Jun. 2006, pp. 1177–1180.
- [6] N.-C. Kuo, B. Zhao, and A. M. Niknejad, "Near-field power transfer and backscattering communication to miniature RFID tag in 65 nm CMOS technology," in *IEEE MTT-S Int. Microw. Symp. Dig.*, May 2016, pp. 1–4.
- [7] A. Safarian, A. Shameli, A. Rofougaran, M. Rofougaran, and F. De Flaviis, "RF identification (RFID) reader front ends with active blocker rejection," *IEEE Trans. Microw. Theory Techn.*, vol. 57, no. 5, pp. 1320–1329, May 2009.
- [8] J.-Y. Jung, C.-W. Park, and K.-W. Yeom, "A novel carrier leakage suppression front-end for UHF RFID reader," *IEEE Trans. Microw. Theory Techn.*, vol. 60, no. 5, pp. 1468–1477, May 2012.
- [9] S. Jung, M. Kim, and Y. Yang, "A reconfigurable carrier leakage canceler for UHF RFID reader front-ends," *IEEE Trans. Circuits Syst. I, Reg. Papers, Reg. Papers*, vol. 58, no. 1, pp. 70–76, Jan. 2011.
- [10] H. L. Lee, D.-H. Park, J.-W. Yu, and M.-Q. Lee, "Compact antenna module with optimized Tx-to-Rx isolation for monostatic RFID," *IEEE Microw. Wireless Compon. Lett.*, vol. 27, no. 12, pp. 1161–1163, Dec. 2017.
- [11] M. Forouzandeh and N. Karmakar, "Self-interference cancellation in frequency-domain chipless RFID readers," *IEEE Trans. Microw. Theory Techn.*, vol. 67, no. 5, pp. 1994–2009, May 2019.
- [12] M. Forouzandeh and N. Karmakar, "Application of wideband differential phase shifters with wide phase range in chipless RFID readers," *IEEE Trans. Microw. Theory Techn.*, vol. 67, no. 9, pp. 3636–3650, Sep. 2019.
- [13] M. Sajid and S. Chiu, "Canceling self-jammer and interfering signals in an RFID system," U.S. Patent 8000674, Aug. 16, 2011.
- [14] R. Rimini, P. D. Heidmann, and J. P. Burke, "Method and apparatus for adaptive non-linear self-jamming interference cancellation," U.S. Patent 8744377, Jun. 3, 2014.
- [15] Y. Ma and E. C. Kan, "Accurate indoor ranging by broadband harmonic generation in passive NLTL backscatter tags," *IEEE Trans. Microw. Theory Techn.*, vol. 62, no. 5, pp. 1249–1261, May 2014.
- [16] Y. Ma, X. Hui, and E. C. Kan, "Harmonic-WISP: A passive broadband harmonic RFID platform," in *IEEE MTT-S Int. Microw. Symp. Dig.*, May 2016, pp. 1–4.
- [17] F. Amato and S. Hemour, "The harmonic tunneling tag: A dual-band approach to backscattering communications," in *Proc. IEEE Int. Conf. RFID Technol. Appl. (RFID-TA)*, Pisa, Italy, Sep. 2019, pp. 244–247.
- [18] X. Gu, L. Guo, S. Hemour, and K. Wu, "Analysis and exploitation of diplexer-based fully passive harmonic transponder for 5G applications," in *IEEE MTT-S Int. Microw. Symp. Dig.*, Dublin, Ireland, Aug. 2018, pp. 1–3.
- [19] X. Gu, N. N. Srinaga, L. Guo, S. Hemour, and K. Wu, "Diplexer-based fully passive harmonic transponder for Sub-6-GHz 5G-compatible IoT applications," *IEEE Trans. Microw. Theory Techn.*, vol. 67, no. 5, pp. 1675–1687, May 2019.
- [20] X. Gu, L. Guo, S. Hemour, and K. Wu, "Novel diplexer-based harmonic transponder for 5G-compatible IoT applications," in *Proc. IEEE Wireless Power Transf. Conf. (WPTC)*, Jun. 2018, pp. 1–4.
- [21] S. Khaledian, F. Farzami, B. Smida, and D. Erricolo, "Two-way backscatter communication tag using a reflection amplifier," *IEEE Microw. Wireless Compon. Lett.*, vol. 29, no. 6, pp. 421–423, Jun. 2019.
- [22] F. Amato, C. W. Peterson, B. P. Degnan, and G. D. Durgin, "Tunneling RFID tags for long-range and low-power microwave applications," *IEEE J. Radio Freq. Identificat.*, vol. 2, no. 2, pp. 93–103, Jun. 2018.
- [23] F. Amato, H. M. Torun, and G. D. Durgin, "RFID backscattering in long-range scenarios," *IEEE Trans. Wireless Commun.*, vol. 17, no. 4, pp. 2718–2725, Apr. 2018.
- [24] F. Farzami, S. Khaledian, B. Smida, and D. Erricolo, "Reconfigurable dual-band bidirectional reflection amplifier with applications in van Atta array," *IEEE Trans. Microw. Theory Techn.*, vol. 65, no. 11, pp. 4198–4207, Nov. 2017.
- [25] F. Farzami, S. Khaledian, B. Smida, and D. Erricolo, "Ultra-low power reflection amplifier using tunnel diode for RFID applications," in *Proc. IEEE Int. Symp. Antennas Propag.*, Jul. 2017, pp. 2511–2512.
- [26] S. Khaledian, F. Farzami, D. Erricolo, and B. Smida, "A full-duplex bidirectional amplifier with low DC power consumption using tunnel diodes," *IEEE Microw. Wireless Compon. Lett.*, vol. 27, no. 12, pp. 1125–1127, Dec. 2017.
- [27] J. Lee and K. Yang, "RF power analysis on 5.8 GHz low-power amplifier using resonant tunneling diodes," *IEEE Microw. Wireless Compon. Lett.*, vol. 27, no. 1, pp. 61–63, Jan. 2017.
- [28] F. Amato, C. W. Peterson, B. P. Degnan, and G. D. Durgin, "A 45 μ W bias power, 34 dB gain reflection amplifier exploiting the tunneling effect for RFID applications," in *Proc. IEEE Int. Conf. (RFID)*, Apr. 2015, pp. 137–144.
- [29] J. Kimionis, A. Georgiadis, A. Collado, and M. M. Tentzeris, "Enhancement of RF tag backscatter efficiency with low-power reflection amplifiers," *IEEE Trans. Microw. Theory Techn.*, vol. 62, no. 12, pp. 3562–3571, Dec. 2014.
- [30] J. Kimionis, M. M. Tentzeris, A. Georgiadis, and A. Collado, "Inkjet-printed reflection amplifier for increased-range backscatter radio," in *Proc. 44th Eur. Microw. Conf.*, Oct. 2014, pp. 5–8.
- [31] J. Kimionis, A. Georgiadis, S. Kim, A. Collado, K. Niotaki, and M. M. Tentzeris, "An enhanced-range RFID tag using an ambient energy powered reflection amplifier," in *IEEE MTT-S Int. Microw. Symp. Dig.*, Jun. 2014, pp. 1–4.
- [32] J. Lee, J. Lee, and K. Yang, "Reflection-type RTD low-power amplifier with deep sub-mW DC power consumption," *IEEE Microw. Wireless Compon. Lett.*, vol. 24, no. 8, pp. 551–553, Aug. 2014.
- [33] P. Chan and V. Fusco, "Full duplex reflection amplifier tag," *IET Microw., Antennas Propag.*, vol. 7, no. 6, pp. 415–420, Apr. 2013.
- [34] A. Lazaro, A. Ramos, R. Villarino, and D. Girbau, "Time-domain UWB RFID tag based on reflection amplifier," *IEEE Antennas Wireless Propag. Lett.*, vol. 12, pp. 520–523, 2013.
- [35] V. Vesterinen, J. Hassel, and H. Seppa, "Tunable impedance matching for josephson junction reflection amplifier," *IEEE Trans. Appl. Supercond.*, vol. 23, no. 3, Jun. 2013, Art. no. 1500104.
- [36] J.-F. Bousquet, S. Magierowski, and G. G. Messier, "A 4-GHz active scatterer in 130-nm CMOS for phase sweep amplify-and-forward," *IEEE Trans. Circuits Syst. I, Reg. Papers*, vol. 59, no. 3, pp. 529–540, Mar. 2012.
- [37] P. Chan and V. Fusco, "Bi-static 5.8 GHz RFID range enhancement using retrodirective techniques," in *Proc. IEEE Eur. Microw. Conf. (EuMC)*, Oct. 2011, pp. 976–979.
- [38] H. I. Cantu, V. F. Fusco, and S. Simms, "Microwave reflection amplifier for detection and tagging applications," *IET Microw., Antennas Propag.*, vol. 2, no. 2, pp. 115–119, Mar. 2008.
- [39] H. Cantu and V. Fusco, "A 21 GHz reflection amplifier MMIC for retro-directive antenna and RFID applications," in *Proc. IET Seminar MM-Wave Products Technol.* London, U.K.: IET, Nov. 2006, pp. 66–70. [Online]. Available: <https://ieeexplore.ieee.org/document/4126091>, doi: 10.1049/ic:20060112.
- [40] S.-J. Chung, S.-M. Chen, and Y.-C. Lee, "A novel bi-directional amplifier with applications in active van atta retrodirective arrays," *IEEE Trans. Microw. Theory Techn.*, vol. 51, no. 2, pp. 542–547, Feb. 2003.
- [41] T.-H. Lin, J. Bito, J. G. D. Hester, J. Kimionis, R. A. Bahr, and M. M. Tentzeris, "On-body long-range wireless backscattering sensing system using Inkjet-/3-D-printed flexible ambient RF energy harvesters capable of simultaneous DC and harmonics generation," *IEEE Trans. Microw. Theory Techn.*, vol. 65, no. 12, pp. 5389–5400, Dec. 2017.
- [42] X. Chen *et al.*, "Long read range Class-3 UHF RFID system based on harmonic backscattering," *Electron. Lett.*, vol. 54, no. 22, pp. 1262–1264, Nov. 2018.
- [43] V. Palazzi, F. Alimenti, P. Mezzanotte, G. Orecchini, and L. Roselli, "Zero-power, long-range, ultra low-cost harmonic wireless sensors for massively distributed monitoring of cracked walls," in *IEEE MTT-S Int. Microw. Symp. Dig.*, Honolulu, HI, USA, Jun. 2017, pp. 1335–1338.

- [44] K. Rasilainen, J. Ilvonen, A. Lehtovuori, J.-M. Hannula, and V. Viikari, "On design and evaluation of harmonic transponders," *IEEE Trans. Antennas Propag.*, vol. 63, no. 1, pp. 15–23, Jan. 2015.
- [45] A. Lazaro, R. Villarino, and D. Girbau, "A passive harmonic tag for humidity sensing," *Int. J. Antennas Propag.*, vol. 2014, Jul. 2014, Art. no. 670345, doi: [10.1155/2014/670345](https://doi.org/10.1155/2014/670345).
- [46] K. Gumber, F. Amato, C. Dejous, and S. Hemour, "Nonlinear negative resistance-based harmonic backscatter," in *IEEE MTT-S Int. Microw. Symp. Dig.*, Los Angeles, CA, USA, Aug. 2020, pp. 603–606.
- [47] S. Hemour *et al.*, "Towards low power high efficiency RF and microwave energy harvesting," *IEEE Trans. Microw. Theory Techn.*, vol. 62, no. 4, pp. 965–976, Apr. 2014.
- [48] C. H. P. Lorenz *et al.*, "Breaking the efficiency barrier for ambient microwave power harvesting with heterojunction backward tunnel diodes," *IEEE Trans. Microw. Theory Techn.*, vol. 63, no. 12, pp. 4544–4555, Dec. 2015.
- [49] A. Al-Khalidi *et al.*, "Resonant tunneling diode terahertz sources with up to 1 mW output power in the J-Band," *IEEE Trans. THz Sci. Technol.*, vol. 10, no. 2, pp. 150–157, Mar. 2020.
- [50] R. J. Hwu, A. Djouadi, and S. C. Lee, "Negative differential resistance (NDR) frequency conversion with gain," *IEEE Trans. Microw. Theory Techn.*, vol. 41, no. 5, pp. 890–893, May 1993.
- [51] F. S. Barnes and G. F. Eiber, "An ideal harmonic generator," *Proc. IEEE*, vol. 53, no. 7, pp. 693–695, Jul. 1965.
- [52] Y. Zhao, S. Hemour, T. Liu, and K. Wu, "Negative resistance-based electronic impedance tuner," *IEEE Microw. Wireless Compon. Lett.*, vol. 28, no. 2, pp. 144–146, Feb. 2018.
- [53] C. C. Hoffins and K. Ishii, "Conditions of oscillation for waveguide mounted tunnel diodes," *IEEE Trans. Microw. Theory Techn.*, vol. 12, no. 2, pp. 176–183, Mar. 1964.
- [54] C. Kidner, I. Mehdi, J. R. East, and G. I. Haddad, "Power and stability limitations of resonant tunneling diodes," *IEEE Trans. Microw. Theory Techn.*, vol. 38, no. 7, pp. 864–872, Jul. 1990.
- [55] C. E. Saavedra, B. R. Jackson, and S. S. K. Ho, "Self-oscillating mixers: A natural fit for active antennas," *IEEE Microw. Mag.*, vol. 14, no. 6, pp. 40–49, Sep. 2013.
- [56] J. Zhang, Y. Wang, and Z. Chen, "Integration of a self-oscillating mixer and an active antenna," *IEEE Microw. Guided Wave Lett.*, vol. 9, no. 3, pp. 117–119, Mar. 1999.
- [57] C. Toker, "Self-oscillating tunnel-diode mixer having conversion gain (Short Papers)," *IEEE Trans. Microw. Theory Techn.*, vol. 20, no. 9, pp. 616–618, Sep. 1972.
- [58] A. Lazaro, D. Girbau, and D. Salinas, "Radio link budgets for UHF RFID on multipath environments," *IEEE Trans. Antennas Propag.*, vol. 57, no. 4, pp. 1241–1251, Apr. 2009.
- [59] J. Lee, J. Lee, and K. Yang, "An on-off mode RTD oscillator operating at extremely low power consumption," *IEEE Trans. Nanotechnol.*, vol. 11, no. 5, pp. 863–865, Sep. 2012.
- [60] J. Wang, A. A. Khalidi, L. Wang, R. Morariu, A. Ofiare, and E. Wasige, "15-Gb/s 50-cm wireless link using a high-power compact III-V 84-GHz transmitter," *IEEE Trans. Microw. Theory Techn.*, vol. 66, no. 11, pp. 4698–4705, Nov. 2018.
- [61] S. Khaledian, F. Farzami, B. Smida, and D. Erricolo, "A power-efficient implementation of in-band full-duplex communication system (ReflectFX)," in *Proc. Int. Symp. Signal, Image, Video Commun. (ISIVC)*, Tunis, Tunisia, Nov. 2016, pp. 242–246.



Karan Gumber (Member, IEEE) was born in Punjab, India, in 1988. He received the M.E. degree in electronics and communication from the University Institute of Engineering and Technology, Panjab University, Chandigarh, India, in 2012, and the Ph.D. degree in electronics and communication from the IIT Roorkee, Uttarakhand, India, in 2019.

He is currently a Post-Doctoral Fellow with the IMS Research Center, University of Bordeaux, Bordeaux, France. His research has been concerned with resonant tunneling diodes, backscattering, RFID, linearization techniques for high power amplifiers, and software defined radios.



Corinne Dejous (Member, IEEE) received the M.S. degree (electronics engineer) from the French Grande École ENSEIRB, Talence, France, in 1991, and the Ph.D. degree in electronics from the University of Bordeaux, Talence, in 1994.

In 1996, she was appointed as an Assistant Professor with the University of Bordeaux, and promoted in 2009 to Full Professor with ENSEIRB-MATMECA / Bordeaux INP, Bordeaux, where she teaches electronic systems and instrumentation, chemical sensors, and microsystems. She leads research at IMS Laboratory (CNRS UMR 5218) in acoustic wave (bio)chemical microsensors and more generally wave-based resonant sensors, her research activities also include wireless microdevices. Major fields of applications aim health and environment purposes. She was the Head of the Research Group Ondes, Talence, from 2011 to 2018. Since 2016, she has been an In-Charge of the IMS Labs' Transverse Topic Environments. She coauthored over 80 publications in international journals or book chapters, 180 communications, delivered many invited talks, and co-supervised 35 research projects. She is also involved in the French Chapter of the IEEE Sensors Council.



Simon Hemour (Senior Member, IEEE) received the B.S. degree in electrical engineering from the University of Grenoble Alpes, Grenoble, France, in 2004, and the M.S. and Ph.D. degrees in optics, optoelectronics, and microwave engineering from the Grenoble Institute of Technology, Grenoble, in 2006 and 2010, respectively.

In 2003, he was with the European Organization for Nuclear Research, Geneva, Switzerland, as a member of the Instrumentation Department, where he was involved in ATLAS experiment on the Large Hadron Collider. From 2006 to 2007, he was a Research Assistant with the Pidstryhach Institute of Applied Problems of Mechanics and Mathematics, National Academy of Science of Ukraine, Lviv, Ukraine. In 2007, he joined the IMEP-LAHC MINATEC Laboratory, Grenoble. From 2011 to 2015, he was with the Poly-Grames Research Center, École Polytechnique de Montréal, Montreal, QC, Canada, where he was coordinating the Wireless Power Transmission and Harvesting Research Group. He joined the Université de Bordeaux, Bordeaux, France, in 2015, where he is currently an Associate Professor, and he leads research in wireless micro energy solutions for IoT and biomedical applications. His current research interests include wireless power transfer and hybrid energy harvesting, backscattering, nonlinear and negative resistance devices, innovative RF measurements, RF interferometry, low power microwave, and millimeter wave conversion circuits, development of RF transponders and sensors for wireless systems and biomedical applications.

Dr. Hemour is a member of the IEEE MTT-25 Wireless Energy Transfer and Conversion Technical Committee and the IEEE MTT-28 Biological Effect and Medical Application Technical Committee. He has been invited to give many invited talks and plenary speeches at various international meetings, conferences and forums, and his pioneering work on low power RF energy harvesting has been highly cited. He was the TPC Chair of the 2018 Wireless Power Transfer Conference (WPTC), and will be the General Chair of the 2022 WPTC. He is part of the Editorial Board of the *Wireless Power Transfer Journal* (Cambridge University Press). He has served as Guest Editor for the *IEEE TRANSACTIONS ON MICROWAVE THEORY AND TECHNIQUES* and the *IEEE Journal of Electromagnetics, RF and Microwaves in Medicine and Biology*.